Article

High Content Analysis of 3D Chondrogenic Spheroids Derived from Primary Cells *In Vitro*

Lucija Voga , Tilen Burnik , Maša Kandušer , Matjaž Jeras , Janja Zupan , Andreja Trojner Bregar *

Posted Date: 22 April 2026

doi: 10.20944/preprints202604.1558.v1

Keywords: primary progenitor cells; chondrogenesis; 3D spheroids; high content analysis; type II collagen; immunofluorescence

 doi:10.20944/preprints202604.1558.v1

Article

High Content Analysis of 3D Chondrogenic Spheroids Derived from Primary Cells *In Vitro*

Lucija Voga [1,2], Tilen Burnik [1,3], Maša Kandušer [3], Matjaž Jeras [1], Janja Zupan [1] and Andreja Trojner Bregar [4,5]*

[1] University of Ljubljana, Department of Clinical Biochemistry, Faculty of Pharmacy, Aškerčeva 7, SI-1000 Ljubljana, Slovenia
[2] University of Ljubljana, Department of Biochemistry, Faculty of Chemistry and Chemical Technology, Večna pot 113, SI-1000 Ljubljana, Slovenia
[3] University of Ljubljana, Institute of Pharmacy, Faculty of Pharmacy, Aškerčeva 7, SI-1000 Ljubljana, Slovenia
[4] Department of Perinatology, Division of Gynecology and Obstetrics, University Medical Centre Ljubljana, Šlajmerjeva 3, 1000 Ljubljana, Slovenia
[5] University of Ljubljana, Faculty of Medicine, Vrazov trg 2, 1000 Ljubljana, Slovenia
* Correspondence: andreja.trojner@kclj.si@; Tel.: 00 386 1522 60 60

Abstract

Background: Primary cells derived from connective tissues contain mesenchymal stem/stromal cell (MSC)–like progenitors with chondrogenic potential relevant for cartilage repair. However, donor- and tissue-specific variability and the lack of robust, high-throughput analytical methods limit their translational use. **Objectives**: This study aimed to develop and optimize a fast, reproducible high-content imaging workflow for quantitative evaluation of chondrogenesis in three-dimensional (3D) spheroids derived from primary cells. **Methods**: Primary human cells isolated from cartilage were chondrogenically differentiated in vitro. A systematic optimization of immunofluorescence staining parameters was performed, including staining platform, enzymatic matrix digestion, non-specific site blocking, membrane permeabilization, and nuclear counterstaining. Type II collagen was detected using an Alexa Fluor 488–conjugated antibody, and spheroids were analyzed using high-content non-confocal imaging. Fluorescence intensities were normalized to spheroid area to account for size-dependent effects. **Results**: Staining directly in imaging plates enabled streamlined high-content analysis. Controlled pepsin-mediated matrix digestion markedly enhanced antibody penetration, while excessive digestion compromised spheroid integrity. Extended bovine serum albumin blocking improved type II collagen signal intensity and homogeneity. Triton X-100 permeabilization increased detection sensitivity but occasionally induced structural disruption in weakly organized control spheroids. The optimized protocol enabled clear discrimination between chondrogenic spheroids and controls, with approximately threefold higher type II collagen signal in chondrogenic samples. **Conclusions**: This study establishes a standardized, high-content imaging–based workflow for quantitative assessment of 3D chondrogenesis from primary cells. The approach provides a rapid, scalable platform with direct relevance for in vitro screening, potency testing, and quality control in cartilage-oriented advanced therapy development.

Keywords: primary progenitor cells; chondrogenesis; 3D spheroids; high content analysis; type II collagen; immunofluorescence

1. Introduction

Articular cartilage injuries and degenerative joint disorders represent a major clinical and socioeconomic challenge due to the inherently limited regenerative capacity of hyaline cartilage. Osteoarthritis (OA), the most prevalent degenerative joint disorder, continues to rise globally, with an estimated 607 million affected individuals and tens of millions of new diagnoses recorded in 2021

 doi:10.20944/preprints202604.1558.v1

alone (Qiao et al. 2025). The increasing life expectancy and prevalence of obesity are expected to further accelerate this trend, contributing to a substantial burden on healthcare systems and compromised quality of life for aging populations ("Osteoarthritis" n.d.).

Primary cells isolated from adult tissues—including bone, adipose tissue, muscle, synovium, and other connective tissues—that exhibit mesenchymal stem/stromal cell (MSC)-like characteristics hold considerable therapeutic promise for OA. Their regenerative capacity, coupled with their immunomodulatory functions, positions them as highly attractive candidates for OA treatment (Campos et al. 2019; Zupan et al. 2021). Building on these biological advantages, recent decades have witnessed the emergence of advanced therapy medicinal products (ATMPs) as a promising avenue for repairing focal cartilage defects and potentially altering disease progression. Autologous chondrocyte–based products such as Spherox® (registered by European Medicines Agency) and MACI® (registered by Food and Drug Agency) are clinically approved ATMPs that utilize primary human chondrocytes cultured ex vivo. Spherox®, comprising spherical aggregates of autologous chondrocytes embedded in their self-produced extracellular matrix, is indicated for treating full-thickness cartilage defects of the femoral condyle and patella (ICRS grade III–IV). Whereas MACI® consists of autologous chondrocytes seeded onto a porcine collagen I/III membrane for treatment of symptomatic cartilage defects of the knee. Despite their clinical success, these ATMPs rely on harvesting and expanding autologous chondrocytes, a process that is frequently limited by donor age, tissue quality, and the intrinsic decline in cellular potency. Age-associated stem cell exhaustion—recognized as a hallmark of aging (Partridge, Deelen, and Slagboom 2018)—compromises not only tissue-resident stem cell pools but also their downstream chondrogenic progenitors (M. P. Murphy et al. 2020). Our previous work demonstrated that patients with OA exhibit diminished colony-forming efficiency and reduced chondrogenic capacity of bone- and muscle-derived mesenchymal stem/stromal cells (MSCs) compared to healthy controls (Čamernik, Mihelič, Mihalič, Haring, et al. 2020; Čamernik, Mihelič, Mihalič, Marolt Presen, et al. 2020). These findings underscore important concerns regarding the suitability of autologous cell sources for therapeutic applications in individuals already affected by degenerative joint pathology. Moreover, they underscore the need for a rapid and reliable method to evaluate the chondrogenic capacity of patient-derived primary cells in vitro prior to their clinical use in cartilage regeneration.

Chondrogenic differentiation of primary cells in vitro can be induced under appropriate cues including transforming growth factor (TGF)-β1/β3, insulin-like growth factor 1, dexamethasone, ascorbate, and insulin, transferrin and selenite supplement (Campos et al. 2019). However, traditional two-dimensional (2D) monolayer culture systems, despite their widespread use, do not recapitulate the native three-dimensional (3D) extracellular matrix (EMC)–rich microenvironment that is essential for promoting and stabilizing chondrogenic lineage commitment. In contrast, 3D culture models such as pellets, hanging drops, organoids, and spheroids offer more physiologically relevant systems that enhance cell–cell interactions, ECM deposition, and lineage-specific differentiation. Spheroids in particular provide controllable, scaffold-free microtissues that mimic aspects of native tissue physiology and have become a central tool for engineering complex 3D tissues (Fennema et al. 2013). These features make 3D models indispensable for studying cartilage formation, evaluating novel regenerative strategies, and developing ATMPs.

Despite advances in 3D culture systems, the field lacks standardized, robust, and high-throughput in vitro assays capable of reliably evaluating the quality of cartilage-like tissue formed by primary cells or MSCs. This gap represents a major bottleneck in ATMP development, where regulatory frameworks require stringent and reproducible potency and quality assessments. Current analytical approaches—such as histology, biochemical ECM quantification, mechanical testing, and gene expression profiling—are often destructive, low-throughput, labor-intensive, and highly operator-dependent. Based on these limitations there is an urgent need for fast, high-content, and reproducible 3D tissue analytics.

Furthermore, conventional methods struggle to capture pellet heterogeneity and dynamic ECM deposition over time, parameters that are critical for ensuring batch comparability and predicting

 doi:10.20944/preprints202604.1558.v1

clinical outcomes in ATMP manufacturing. High-content imaging and automated image analysis offer a promising solution; however, validated protocols for 3D chondrogenic pellets remain scarce.

The objective of this study was to develop and optimize a fast, robust, and high-throughput high-content imaging workflow for evaluating type II collagen–rich neocartilage formation in 3D chondrogenic pellets generated from primary somatic cells or MSCs. Following standardized culture conditions for pellet formation, we have implemented and optimized immunofluorescence staining for type II collagen and validated automated image analysis pipelines for quantitative assessment. The resulting method enables efficient evaluation of multiple pellets simultaneously, while requiring minimal cell numbers, and offering a scalable and reproducible platform for assessing chondrogenic capacity in vitro. The high content analysis thus provides a possible solution to a critical methodological gap in ATMP development by providing a rapid and reliable approach for assessing cartilage quality during early-stage screening and process development.

2. Materials and Methods

2.1. Human Tissue Samples

Human articular cartilage was obtained from two donors undergoing routine total or partial knee arthroplasty at Department of Orthopedic Surgery at University Medical Centre Maribor. Approval for this study was obtained from the National Medical Ethics Committee of the Republic of Slovenia (reference number: 0120-268/2020/3). Written informed consent was obtained from all the patients included in the study.

2.2. Primary Human Cell Culture

Human articular cartilage was obtained from donors undergoing total or partial knee arthroplasty, in accordance with the National medical ethics committee approval No. 0120-268/2020/3. Cartilage explants were transferred to low glucose Dulbecco's modified Eagle's medium (LG-DMEM; Biowest), supplemented with 1% glutamine and 2% penicillin and streptomycin (all Biowest), without serum and processed at room temperature within 24 hours. All isolation procedures and in vitro experiments were performed at Faculty of Pharmacy, University of Ljubljana. Primary chondrocytes were isolated following a previously described protocol (Žigon-Branc et al. 2018). Briefly, cartilage biopsies (approximately 1-2 cm^3) were minced and digested in LG-DMEM containing 1 mg/mL collagenase from Clostridium histolyticum (C1639, Sigma-Aldrich) at 37 °C for 24 h with constant agitation. Isolated cellular fractions were seeded at passage (p) 0 in T175 flasks using LG-DMEM supplemented with 10% fetal bovine serum (Gibco, Cat. No. 10270106 in LOT 42F9681K), 1% glutamine and 2% penicillin and streptomycin (all Biowest). Once cultures reached 80-90% confluence, cells were detached with trypsin-EDTA and cryopreserved in FBS with 10% dimethyl sulfoxide. Cryopreserved cells were later thawed and culture expanded to obtain sufficient quantities appropriate for optimization of the current analysis. Cell morphology and confluence were monitored and imaged using Evos XL inverted microscope (LifeTechnologies).

2.3. Chondrogenic Differentiation

Chondrogenic differentiation in vitro was performed as previously described (Čamernik, Mihelič, Mihalič, Haring, et al. 2020; Čamernik, Mihelič, Mihalič, Marolt Presen, et al. 2020; Haring and Zupan 2022; Zupan and Stražar 2024). Briefly, spheroids were created by centrifuging 100.000 cells per spheroid at 300 × g for 10 minutes. The resulting cell pellets were incubated overnight in 15-mL conical tubes at 37 °C in a humidified atmosphere containing 5% CO_2, to allow spheroid formation. The following day, in treated spheroids the supernatant was carefully removed and replaced with 500 µL of chondrogenic differentiation medium composed of high-glucose DMEM (Biowest), 100 nM dexamethasone (Sigma), 50 µg/mL 2-Phospho-L-ascorbic acid trisodium salt (Sigma), 1% insulin-transferrin-selenium (Sigma), 10 ng/ml TGF-β1 (Gibco), and antibiotic-

 doi:10.20944/preprints202604.1558.v1

antimycotic solution (Biowest). On the other hand, control spheroids received 500 µL of non-differentiation medium, containing the same components as chondrogenic differentiation medium except for the chondrogenic inducer TGF-β1. Spheroids were cultured for 21 days, with media changes performed every two to three days.

2.4. Optimizing Immunofluorescence Staining Protocol

To optimize the immunofluorescence staining protocol, spheroids were collected from the culture medium and washed with PBS. A subset of samples was transferred to 96-well Revvity CellCarrier Spheroid ULA plates (Revvity) for staining and imaging, while the remaining spheroids were kept in 15-mL conical tubes to evaluate an alternative staining platform. Spheroids were fixed in 200 µL of 10% neutral buffered formalin (Sigma-Aldrich) for 10 minutes at room temperature, followed by two washes with Dulbecco's PBS (Sigma-Aldrich). To enable controlled antigen retrieval, samples were equilibrated in 200 µl of 0.2 M HCl (Sigma) for 5 minutes at 37 °C, followed by incubation with 0.5 g/L pepsin (Roche) in 0.2 M HCl for 10–30 minutes at 37 °C. Digestion was stopped by incubation in 200 µL of Milli-Q water for 5 minutes at room temperature, followed by a PBS wash. Cell membranes were permeabilized three times with 200 µL of 0.2% Triton X-100 (Sigma) for 5 minutes at room temperature. Non-specific binding sites were then blocked with 200 µL of 1% bovine serum albumin (BSA, Sigma-Aldrich) in 0.2% Triton X-100 for 30–45 minutes at room temperature, followed by a PBS wash. Spheroids were incubated with 200 µL of anti-type II collagen antibody conjugated with Alexa Fluor (AF) 488 (SouthernBiotech), diluted 1:100 in PBS, for 24 hours at 2–8 °C in the dark. After primary antibody incubation, samples were washed twice with PBS and once with 0.2% Triton X-100 in PBS for 10 minutes at room temperature. Nuclear staining was performed using 200 µL of Hoechst 33342 (Thermo Fisher), diluted 1:2000 in PBS, for 20 minutes or 1 hour at room temperature in the dark, followed by two PBS washes. Spheroids initially kept in 15-mL conical tubes were transferred to imaging plates prior acquisition. For one sample, Triton X-100 was omitted, and all corresponding steps were performed using PBS.

2.5. High-Content Imaging Acquisition and Analysis

High content imaging was performed using the Revvity Operetta® CLS™ system controlled by Harmony™ software (version 5.2.2). Spheroids were imaged in 96-well Revvity CellCarrier Spheroid ULA plates using a 10× air objective (NA 0.3) in a non-confocal mode. Acquisition settings included a two-peak autofocus, a camera region of interest of 2160 × 2160 pixels, and 2 × 2 binning. A single acquisition channel was configured to capture AF 488, Hoechst 33342, and brightfield signals. AF 488 was detected using 460–490 nm excitation and 500–550 nm emission, with an exposure time of 15 ms and 30% illumination power. Hoechst 33342 was acquired using 355-385 nm excitation and 430-500 nm emission, with an exposure time of 5 ms and 4% illumination power. Brightfield images were acquired simultaneously within the same channel using a 6 ms and 5% illumination power. Z-stacks were acquired from 0.0 µm with a step size of 20.0 µm across 15 planes, covering the entire spheroid volume.

Image analysis was performed using Harmony™ software by defining an automated analysis sequence. Only Channel Group 1 was selected as the input for all processing steps. Z-stack processing was carried out using maximum intensity projection to generate a global image with 2x2 binning. The spheroid region was identified using the *Find Image Region* function based on the AF 488 signal intensity, which was present throughout the ECM. The region of interest was defined using an absolute threshold with a lower intensity limit of 4000, to eliminate the background, and no upper limit. Object splitting was enabled to separate distinct regions where applicable. Fluorescence quantification for both dyes was performed using the *Calculate Intensity Properties* function applied to the identified spheroid region. Extracted parameters included mean intensity, standard deviation, and coefficient of variation. Spheroid morphology was assessed using the *Calculate Morphology Properties* module to obtain measurements of cross-sectional area, roundness, perimeter, width,

 doi:10.20944/preprints202604.1558.v1

length, and width-to-length ratio. All parameters, along with the number of detected objects were compiled using the *Define Results* step to generate a complete output dataset.

2.6. Statistical Analysis

Intensities (global) for AF 488 and Hoechst 33342 and spheroid areas were used to calculate the normalized intensities using the following formula: (AF 488 or Hoechst 33342 intensity) / (1/Spheroid Area). The results are expressed as the mean ± standard derivation (SD). The schematic representation of the study is shown in Figure 1. Figures were created using BioRender (BioRender.com).

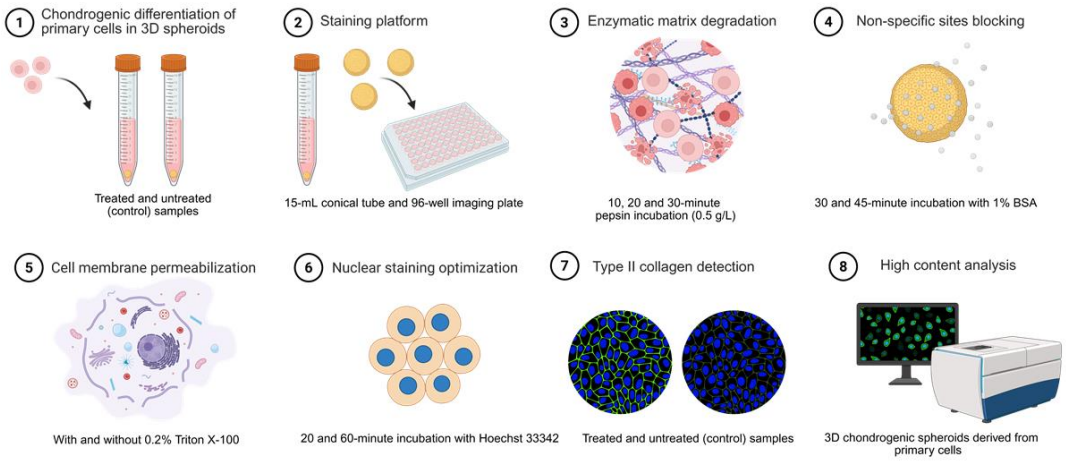

Figure 1. The schematic representation of the study. Created in BioRender. Zupan, J. (2026). https://BioRender.com/gv2ece0.

3. Results

3.1. Experimental Design and Immunostaining Parameters

To adapt immunofluorescence protocols from conventional 2D cultures to 3D spheroid models, we systematically optimized multiple staining parameters, in particular the staining platform, enzymatic matrix degradation, non-specific sites blocking, cell membrane permeabilization, nuclear staining and type II collagen detection. An overview of the experimental design, including sample identifiers is provided in Table 1.

Table 1. Parameters used for the optimization of the immunostaining protocol.

Sample ID	Staining platform	Pepsin matrix digestion	Non-specific sites blocking	Membrane permeabilization	Hoechst 3342 nuclear staining	Chondrogenic treatment
1	15 ml tube	no	no	no	20 min	treated
2	15 mL tube	no	BSA 45 min	Triton X-100	20 min	treated
3	15 mL tube	10 min	BSA 45 min	Triton X-100	20 min	treated
4	15 mL tube	20 min	BSA 45 min	Triton X-100	20 min	treated
5	15 mL tube	30 min	BSA 45 min	Triton X-100	20 min	treated
6	imaging plate	no	no	no	no	treated
7	imaging plate	10 min	BSA 45 min	Triton X-100	20 min	treated
8	imaging plate	20 min	BSA 30 min	Triton X-100	20 min	treated
9	imaging plate	20 min	BSA 45 min	Triton X-100	60 min	treated
10	imaging plate	20 min	BSA 45 min	Triton X-100	60 min	treated
11	imaging plate	20 min	BSA 30 min	Triton X-100	60 min	treated
12	imaging plate	20 min	BSA 30 min	Triton X-100	60 min	treated

 doi:10.20944/preprints202604.1558.v1

13	imaging plate	20 min	BSA 45 min	no	20 min	treated
14	imaging plate	20 min	BSA 45 min	Triton X-100	20 min	treated
C1	imaging plate	20 min	BSA 45 min	Triton X-100	20 min	control

Primary cells for Samples ID 1 to 7 were obtained from donor 2, whereas Samples ID 8 to 14 and C1 were obtained from donor 3.

A range of staining platforms, fixation, blocking, permeabilization, and nuclear counterstaining conditions were evaluated to determine their effects on staining quality and signal acquisition. Key variables included the presence or absence of pepsin digestion, BSA-based blocking, Triton X-100 permeabilization, and variations in incubation times. This systematic assessment allowed the identification of staining parameters compatible with the structural complexity of 3D spheroids.

3.2. Staining Platform

To identify the optimal staining platform for high-content analysis of 3D chondrogenic spheroids, samples were processed either in 15-mL conical tubes or directly in a 96-well imaging plate. Representative fluorescence images of each platform illustrating signal distribution and dye penetration for the spheroid volume are shown in Figure 2.

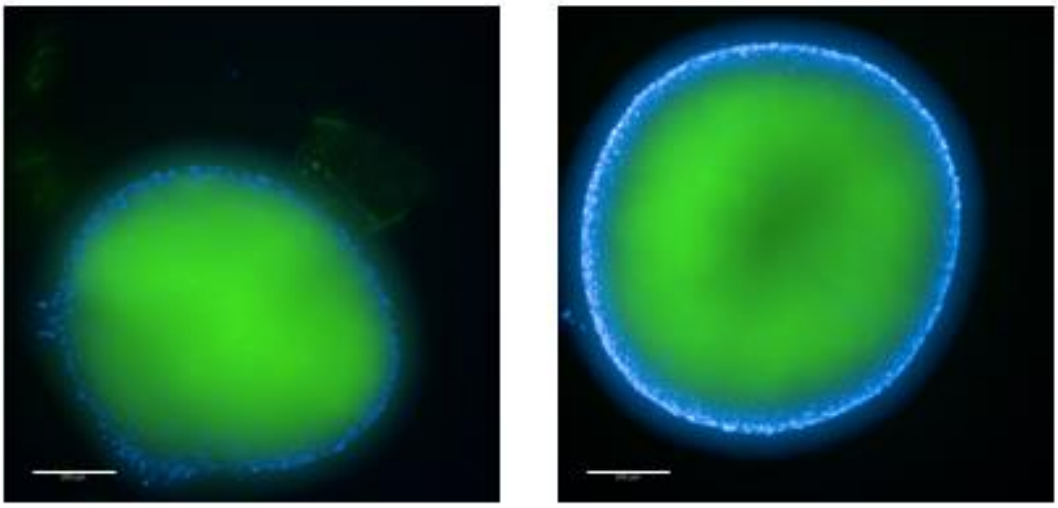

(**a**) (**b**)

Figure 2. Comparison of staining platforms. Sample 3 was stained in 15-mL conical tube (**a**), and sample 7 in 96-well imaging plate (**b**). In both samples, type II collagen (AF 488, green) signal exhibited a comparable distribution pattern, with distinct nuclei (Hoechst, blue) signal visible even within the spheroid core. Sample in (**a**) shows slightly irregular morphology with a visible adhesion site on the lower left side of the spheroid. Images were acquired and displayed using identical settings. Scale bar represents 200µm.

Quantitative fluorescence intensity measurements for AF 488 and Hoechst 33342 are summarized in Table 2.

Table 2. Analysis of fluorescence in samples used for optimization of the staining platform.

			AF 488			Hoechst 33342		
Sample ID	**Staining platform**	**Spheroid area [mm²]**	**Intensity**	**Normalized intensity**	**CV [%]**	**Intensity**	**Normalized intensity**	**CV [%]**
3	15 mL tube	0.63	8081 ± 4186	5111 ± 2648	51.8	667 ± 141	422 ± 89	21.1
7	imaging plate	0.88	7771 ± 3746	6876 ± 3315	48.2	1070 ± 418	947 ± 370	39.1

 doi:10.20944/preprints202604.1558.v1

Values for fluorescent intensities of Alexa Fluor (AF) 488 and Hoechst 33342 are shown as mean ± standard deviation (SD) and coefficient of variation (CV).

Mean and variability of AF 488 fluorescence intensity was higher if spheroids were processed directly in 96-well imaging plates than in 15-mL conical tubes. Also, Hoechst 33342 intensity was higher in the imaging plate than in the conical tube, albeit with greater variability. Notably, spheroids stained in conical tubes often exhibited a visible attachment point to the plastic wall, leading to more irregular and distorted morphologies within an otherwise spherical structure. In contrast, staining directly in imaging plates better preserved their rounded shape (Figure 3).

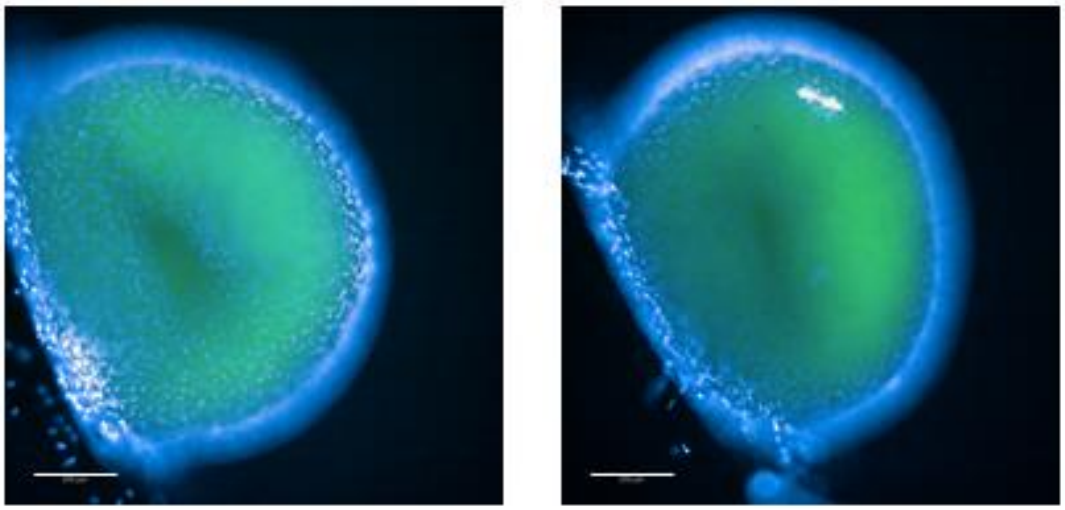

(**a**) (**b**)

Figure 3. Morphological alterations of spheroids stained in 15-mL conical tubes. Representative image of spheroids of samples 4 (**a**) and 5 (**b**) processed in 15-mL conical tubes. These spheroids exhibit a distinct single adhesion point at the site of contact with the tube wall, producing localized irregularity within an otherwise spherical structure. Images were acquired and displayed using identical settings. Scale bar represents 200µm.

3.3. Enzymatic Matrix Degradation

Pepsin was selected for enzymatic matrix degradation. Three pepsin incubation times were evaluated to determine the optimal antigen retrieval and matrix degradation enabling maximal penetration of AF 488-conjugated anti-collagen II antibodies into the spheroid core. Incubation durations of 10, 20, and 30 minutes were tested, along with no-pepsin controls, one without (sample 1) and one with blocking non-specific binding sites (sample 2). The quantitative results are summarized in Table 3.

Table 3. Analysis of fluorescence in samples used for optimization of pepsin treatment.

			AF 488			Hoechst 33342		
Sample ID	**Pepsin treatment [min]**	**Spheroid area [mm²]**	**Intensity**	**Normalized intensity**	**CV [%]**	**Intensity**	**Normalized intensity**	**CV [%]**
1	no-pepsin control	0.86	5275 ± 2615	4512 ± 2236	49.6	722 ± 234	618 ± 200	32.4
2	no-pepsin control	0.99	5121 ± 2339	5092 ± 2326	45.7	595 ± 170	592 ± 169	28.6
3	10	0.63	8081 ± 4186	5111 ± 2648	51.8	667 ± 141	422 ± 89	21.1
4	20	0.87	6406 ± 2882	5583 ± 2511	45.0	687 ± 185	599 ± 161	26.9

 doi:10.20944/preprints202604.1558.v1

5	30	0.80	6452 ± 3217	5169 ± 2577	49.9	659 ± 198	528 ± 159	30.0

Values for fluorescent intensities of Alexa Fluor (AF) 488 and Hoechst 33342 are shown as mean ± standard deviation (SD) and coefficient of variation (CV).

Diffusion-dependent steps in the staining protocol, including pepsin incubation, are strongly influenced by spheroid size. This is the reason we excluded the smallest sample, i.e. sample 3, from the analysis. Its exclusion was primarily justified by the likelihood that pepsin would penetrate more rapidly and extensively in the smaller spheroid during the fixed incubation time, resulting in disproportionately greater matrix digestion relative to larger spheroids. Sample 2, which did not undergo pepsin treatment, also differed in spheroid size. However, because it was not subjected to pepsin-mediated degradation, it was not excluded from the analysis. Therefore, among the four remaining spheroids, clear differences were observed between conditions with and without pepsin treatment. Intensity of AF 488 signal was consistently higher in spheroids treated with pepsin compared to those without treatment. Visual inspection further indicated that a 30-minute incubation induced detachment of some peripheral cells, suggesting over-digestion at longer incubation times (Figure 4).

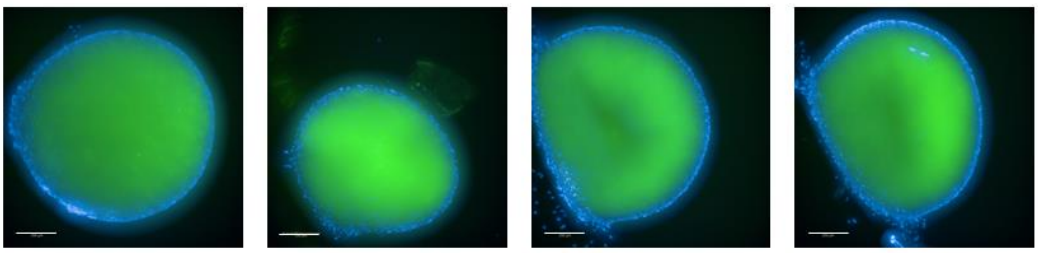

(**a**) (**b**) (**c**) (**d**)

Figure 4. Comparison of spheroid morphology following different durations of pepsin digestion. Sample 2 (**a**) was not exposed to pepsin, whereas sample 3 (**b**) was pepsin-treated for 10 minutes, sample 4 (**c**) for 20 minutes, and sample 5 (**d**) for 30 minutes. Sample 3 (**b**) exhibits a visibly smaller spheroid diameter compared with the other three samples. In samples 4 (**c**) and 5 (**d**), partial detachment of peripheral cells is evident, predominantly on the side that had been in contact with the plastic tube during incubation. All images were acquired and displayed using identical settings. Scale bar represents 200μm.

3.4. Non-Specific Sites Blocking

To determine the optimal duration for blocking non-specific binding sites, two BSA incubation times, i.e. 30 and 45 minutes-were tested. Samples 9–12 were subjected to an extended Hoechst 33342 staining step (60 minutes), whereas samples 8 and 14 were processed using a 20-minute nuclear staining procedure. Consequently, comparisons were made only between samples processed under identical staining conditions. A summary of quantitative results is presented in Table 4.

Table 4. Analysis of fluorescence in samples used for optimization of BSA incubation time.

			AF 488			Hoechst 33342		
Sample ID	**BSA incubation [min]**	**Spheroid area [mm²]**	**Intensity**	**Normalized intensity**	**CV [%]**	**Intensity**	**Normalized intensity**	**CV [%]**
14	45	0.83	9152 ± 4875	7614 ± 4056	53.3	1772 ± 497	1474 ± 414	28.1
8	30	0.85	5922 ± 2835	5049 ± 2417	47.9	1727 ± 499	1472 ± 425	28.9

 doi:10.20944/preprints202604.1558.v1

9	45	0.42	11751 ± 3494	4945 ± 1471	29.7	3429 ± 851	1443 ± 358	24.8
10	45	0.47	10379 ± 2786	4865 ± 1306	26.8	2438 ± 767	1143 ± 360	31.5
11	30	0.52	8275 ± 3665	4329 ± 1917	44.3	2188 ± 1164	1145 ± 609	53.2
12	30	0.59	8405 ± 3694	5000 ± 2198	44.0	3376 ± 1043	2008 ± 621	30.9

Values of fluorescent intensities for Alexa Fluor (AF) 488 and Hoechst 33342 are shown as mean ± standard deviation (SD) and coefficient of variation (CV).

Under standard nuclear staining conditions, shortening the BSA incubation from 45 minutes (sample 14, Figure 5a) to 30 minutes (sample 8, Figure 5b) led to a reduction in mean AF 488 intensity, whereas Hoechst 33342 intensity remained comparable between the two conditions. The coefficient of variation (CV) for AF 488 was similar between the two conditions.

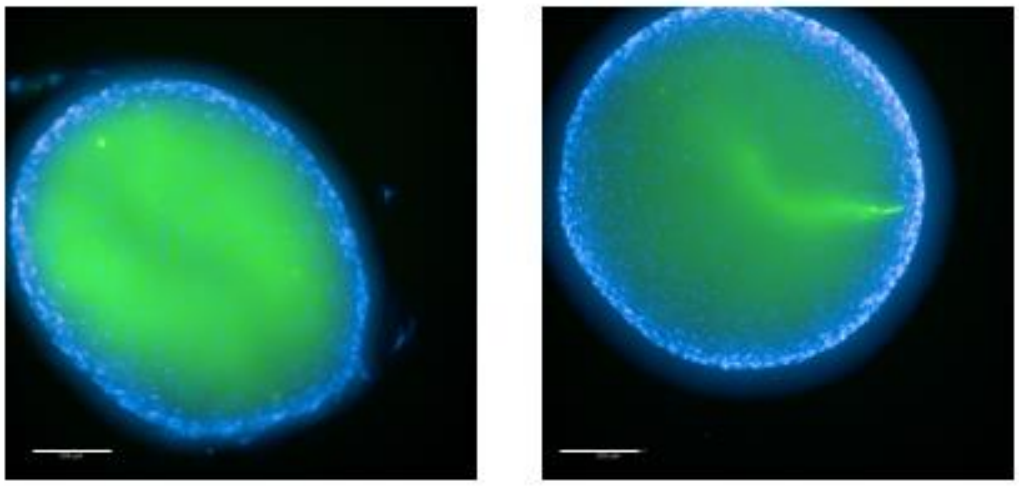

(**a**) (**b**)

Figure 5. Comparison of different BSA incubation times. (**a**) Sample 14 with 45 minutes BSA incubation time and (**b**) sample 8 with 30 minutes BSA incubation time. Images were acquired and displayed using identical settings. Scale bar represents 200µm.

Within the extended nuclear staining set, spheroids incubated with BSA for 45 minutes (samples 9 and 10, Figures 6a and 6b) and those incubated for 30 minutes (samples 11 and 12, Figures 6c and 6d) showed no difference in AF 488 mean intensities. The 45-minute incubation was associated with lower CV of AF 488 intensity compared with 30-minute incubation time, indicating more homogenous staining. Hoechst 33342 intensities did not vary with BSA incubation time across the samples.

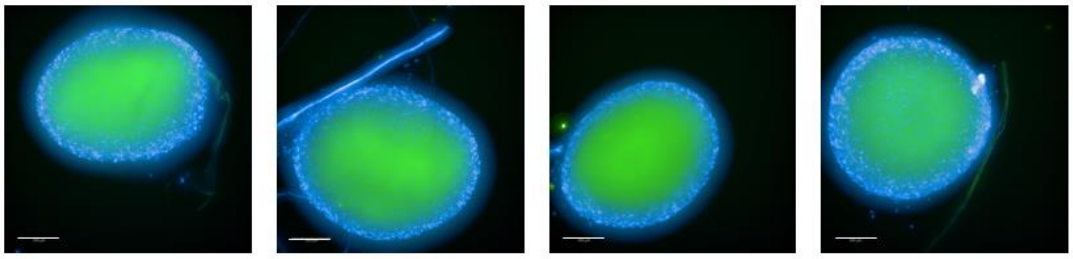

(**a**) (**b**) (**c**) (**d**)

 doi:10.20944/preprints202604.1558.v1

Figure 6. Comparison of different BSA incubation times with an extended Hoechst 33342 incubation time. Samples 9 (**a**) and 10 (**b**) with 45 minutes BSA incubation time. Samples 11 (**c**) and 12 (**d**) with 30 minutes BSA incubation time. Images were acquired and displayed using identical settings. Scale bar represents 200µm.

3.5. Cell Membrane Permeabilization

To assess whether the protocol could be optimized to better preserve spheroid morphology while eliminating unnecessary chemical exposure, Triton X-100 was omitted in one staining condition (sample 13), where it was excluded from all steps and replaced with PBS. Whereas all the other steps) were carried out under standard staining conditions (Table 5) in the same manner as with the sample including Triton X-100 (sample 14).

Table 5. Analysis of fluorescence in samples used for optimization of permeabilization.

			AF 488			Hoechst 33342		
Sample ID	**Triton X-100**	**Spheroid area [mm²]**	**Intensity**	**Normalized intensity**	**CV [%]**	**Intensity**	**Normalized intensity**	**CV [%]**
13	no Triton X-100 control	0.82	6548 ± 2494	5396 ± 2055	38.1	1502 ± 785	1238 ± 647	52.3
14	with Triton X-100	0.83	9152 ± 4875	7614 ± 4056	53.3	1772 ± 497	1474 ± 414	28.1

Values for fluorescent intensities of Alexa Fluor (AF) 488 and Hoechst 33342 are shown as (normalized) mean ± standard deviation (SD) and coefficient of variation (CV).

The exclusion of Triton X-100 from the staining protocol resulted in a marked reduction in fluorescence intensity for both AF 488 and Hoechst 33342 (Figure 7), indicating decreased staining efficacy under non-permeabilizing conditions.

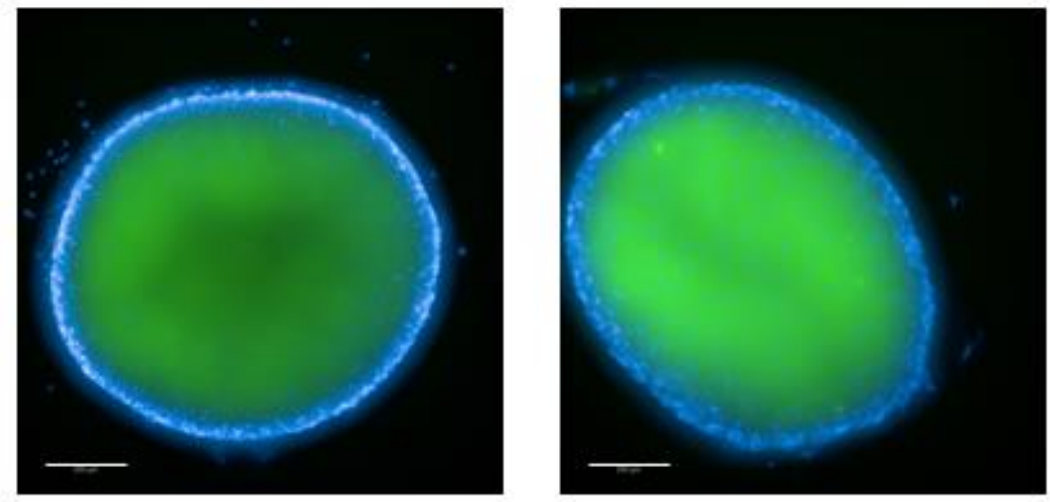

(**a**) (**b**)

Figure 7. Effect of Triton X-100 on fluorescence staining. Representative images obtained using a staining protocol excluding (**a**) or including Triton X-100 (**b**). Images were acquired and displayed using identical settings. Scale bar represents 200µm.

3.6. Nuclear Staining

To determine whether prolonged incubation with Hoechst 33342 enhances nuclear staining within the spheroid core, incubation periods of 20 and 60 minutes were compared. The analysis was performed across two independent experimental sets. In the first one, sample 8 (20-minute incubation, Figure 8a) was compared exclusively with samples 11 and 12 (60-minute incubation, Figures 8b and 8c). In the second set, sample 14 (20-minute incubation, Figure 9a) was compared

 doi:10.20944/preprints202604.1558.v1

exclusively with samples 9 and 10 (60-minute incubation, Figures 9b and 9c). Cross comparisons between the two experimental sets were not performed, as the spheroids were subjected to different staining procedures.

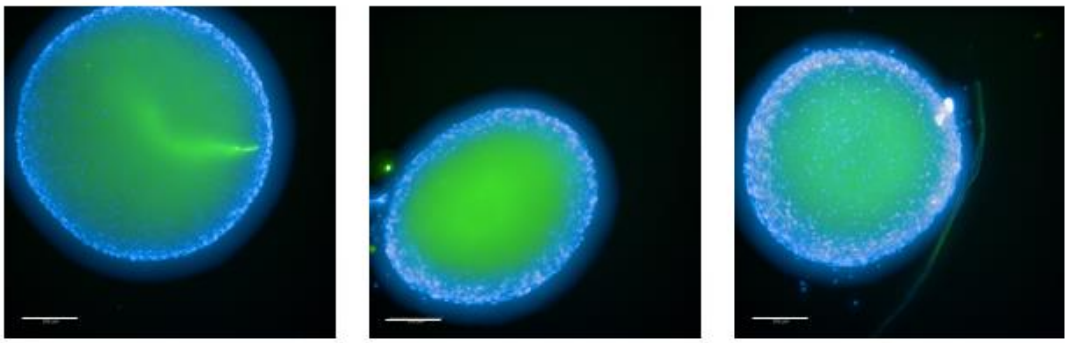

(**a**) (**b**) (**c**)

Figure 8. Comparison of different Hoechst 33342 incubation times following a 30-minute BSA incubation. Sample 8 (**a**) was incubated with Hoechst 33342 for 20 minutes, whereas samples 11 (**b**) and 12 (**c**) were incubated for 60 minutes. Images were acquired and displayed using identical settings. Scale bar represents 200µm.

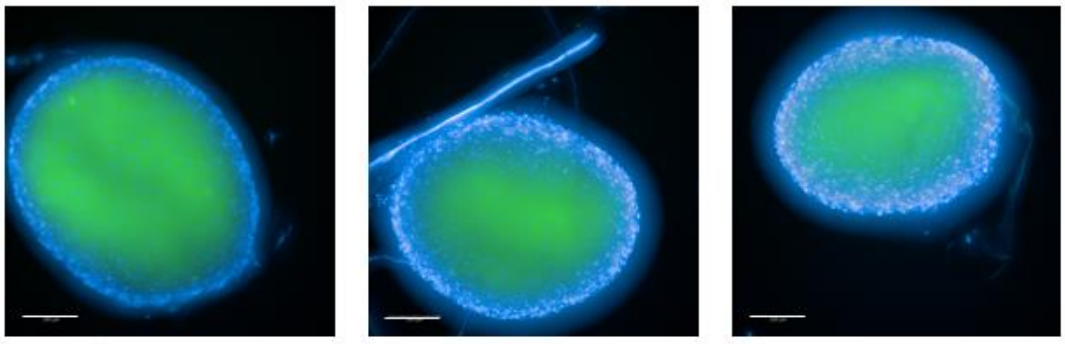

(**a**) (**b**) (**c**)

Figure 9. Comparison of different Hoechst 33342 incubation times following a 45-minute BSA incubation. Sample 14 (**a**) was incubated with Hoechst 33342 for 20 minutes, whereas samples 9 (**b**) and 10 (**c**) were incubated for 60 minutes. Images were acquired and displayed using identical settings. Scale bar represents 200µm.

Increasing the incubation time with Hoechst 33342 did not affect AF 488 intensity. Therefore, this parameter was not considered relevant for further analysis. Since the fluorescence intensity of Hoechst 33342 can scale with spheroid size due to dye concentration within the spheroid, normalized intensities were compared.

Table 6. Analysis of fluorescence in samples used for optimization of Hoechst staining time.

			AF 488			Hoechst 33342		
Sample ID	**Hoechst 33342 [min]**	**Spheroid area [mm²]**	**Intensity**	**Normalized intensity**	**CV [%]**	**Intensity**	**Normalized intensity**	**CV [%]**
8	20	0.85	5922 ± 2835	5049 ± 2417	47.9	1727 ± 499	1472 ± 425	28.9
11	60	0.52	8275 ± 3665	4329 ± 1917	44.3	2188 ± 1164	1145 ± 609	53.2
12	60	0.59	8405 ± 3694	5000 ± 2198	44.0	3376 ± 1043	2008 ± 621	30.9

 doi:10.20944/preprints202604.1558.v1

14	20	0.83	9152 ± 4875	7614 ± 4056	53.3	1772 ± 497	1474 ± 414	28.1
9	60	0.42	11751 ± 3494	4945 ± 1471	29.7	3429 ± 851	1443 ± 358	24.8
10	60	0.47	10379 ± 2786	4865 ± 1306	26.8	2438 ± 767	1143 ± 360	31.5

Values of fluorescent intensities for Alexa Fluor (AF) 488 and Hoechst 33342 are shown as mean ± standard deviation (SD) and coefficient of variation (CV).

Although extended incubation resulted in higher raw Hoechst 33342 fluorescence, normalization to spheroid size indicated that this increase was primarily driven by differences in spheroid size rather than improved nuclear staining within the spheroid core under the tested conditions.

3.7. Type II Collagen Detection

To assess the effectiveness of the optimized protocol to detect type II collagen, a main component of the hyaline cartilage, samples treated with chondrogenic media were compared with controls, i.e. samples cultured without TGF-β1.

During the staining protocol, control sample C1 separated into two fragments (Figure 10), an event that occurred during the Triton X-100 permeabilization step. Despite this fragmentation, the sample was subsequently processed according to the original protocol without modifications, as the overall integrity of the fragments remained sufficient for downstream analysis.

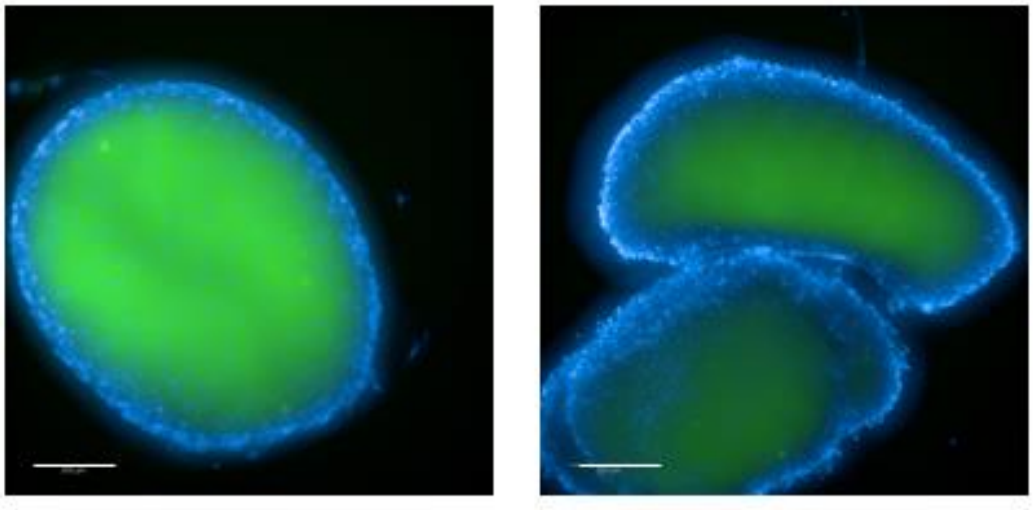

(**a**) (**b**)

Figure 10. Comparison between a sample undergoing chondrogenic differentiation (**a**) and a control sample cultured without chondrogenic induction (**b**). The control sample C1 fragmented during staining protocol. Images were acquired and displayed using identical settings. Scale bar represents 200μm.

The results of this comparison are summarized in Table 8. The mean intensity of AF 488 was approximately three-fold higher in sample 14 undergoing chondrogenic differentiation compared with control (sample C1), while the CV was comparable between the two conditions. In contrast, both, the mean intensity and CV of Hoechst 33342 were higher in control than in the treated sample. To assess the potential contribution of autofluorescence to the AF 488 channel, sample 6 was fixed but not subjected to staining protocol. Sample exhibited relatively high AF 488 signal indicating substantial background fluorescence in this channel. However, in comparison with the AF 488 intensity of the chondrogenic sample, the control displayed almost 3-times lower intensity (Table 8).

 doi:10.20944/preprints202604.1558.v1

Table 8. Analysis of fluorescence in samples undergoing chondrogenic differentiation.

			AF 488			Hoechst 33342		
Sample ID	**Chondrogenic media**	**Spheroid area [mm²]**	**Intensity**	**Normalized intensity**	**CV [%]**	**Intensity**	**Normalized intensity**	**CV [%]**
14	treated	0.83	9152 ± 4875	7614 ± 4056	53.3	1772 ± 497	1474 ± 414	28.1
C1	control	0.81	3409 ± 1734	3000 ± 1525	50.9	2497 ± 1217	2197 ± 1071	48.7
6	treated	0.64	4412 ± 800	2830 ± 513	18.0	242 ± 31	155 ± 20	12.6

Values for fluorescent intensities of Alexa Fluor (AF) 488 and Hoechst 33342 are shown as mean ± standard deviation (SD) and coefficient of variation (CV).

4. Discussion

Articular cartilage injuries and OA present a major clinical challenge due to the limited regenerative capacity of hyaline cartilage and the declining potency of autologous cell sources in affected and aging patients. Although 3D chondrogenic culture systems are increasingly used to model cartilage formation and support ATMP development, there is a lack of standardized, robust, and high-throughput in vitro assays for reliably assessing cartilage-like tissue quality. In the current study, we developed and optimized a fast, reproducible, high-content imaging–based workflow to quantitatively evaluate type II collagen–rich neocartilage formation in 3D chondrogenic pellets derived from primary cells. We systematically evaluated several experimental parameters (Figure 1), including the staining platform (15-mL conical tube versus 96-well imaging plate), enzymatic matrix degradation (no pepsin versus varying pepsin incubation times), BSA blocking (no BSA versus different incubation times), permeabilization (absence or presence of Triton X-100), nuclear staining (absence or presence of Hoechst 33342), and the capacity to detect type II collagen (chondrogenically differentiated 3D spheroids versus control samples). The readouts for all parameters tested were AF488 and Hoechst 33342 fluorescence intensities, normalized to spheroid area. Diffusion and enzymatic penetration strongly depend on spheroid size: smaller spheroids possess shorter diffusion distances and a higher surface-area-to-volume ratio, rendering them more susceptible to rapid and extensive enzymatic degradation under identical incubation conditions. As previously reported, this size dependency can artificially enhance staining intensity in smaller spheroids relative to larger ones, potentially confounding comparative analyses if spheroid size is not controlled or accounted for during data interpretation (Goodman, Olive, and Pun 2007; Im et al. 2019). Based on these considerations, we used normalized fluorescence intensities in our study.

Our results showed that the first parameter, i.e. the choice of staining platform had effect on signal intensity, as 96-well imaging plates platform produced higher fluorescence outcomes. Notably, spheroids stained in conical tubes often exhibited a visible attachment point to the plastic wall, leading to more irregular and distorted morphologies within an otherwise spherical structure. In contrast, staining directly in imaging plates better preserved their rounded shape. However, despite these morphological irregularities observed in conical tubes, this effect was not considered critical and did not strongly impact our decision-making process. 96-well imaging plates nonetheless offered a clear practical advantage, including improved handling, compatibility with high-content imaging and analysis, and better preservation of spheroid morphology. Consequently, 96-well imaging plates were selected for subsequent experiments.

The second evaluated parameter, i.e. the enzymatic matrix digestion, however showed significant effect on AF 488 signal intensity. It is well-recognized that efficient penetration of staining reagents into chondrogenic spheroids remains a persistent technical challenge due to dense ECM and tightly packed cellular architecture that characterize these 3D systems. In particular, cartilaginous spheroids exhibit high contents of proteoglycans and collagen, which substantially restrict the diffusion of large macromolecules such as antibodies (~150 kDa), effectively creating a diffusion

 doi:10.20944/preprints202604.1558.v1

barrier within the spheroid interior (Im et al. 2019; Didomenico, Lintz, and Bonassar 2018). Importantly, the improved antibody signal observed following pepsin treatment suggests that insufficient matrix digestion may lead to underestimation of protein expression in spheroid cores, a limitation that is often overlooked in qualitative and quantitative immunostaining analyses of 3D models. Enzymatic digestion of ECM components is therefore frequently required to enable deeper penetration and achieve homogeneous antibody labeling throughout the spheroid volume. Our results show that the inclusion of a pepsin digestion step (both 20- and 30-minute) significantly enhances the penetration of AF 488–conjugated anti-type II collagen antibody into chondrogenic spheroids. This observation aligns well with prior studies showing that targeted enzymatic degradation of ECM components can markedly improve macromolecular diffusion in 3D culture systems, resulting in more uniform and representative staining patterns (Didomenico, Lintz, and Bonassar 2018; Goodman, Olive, and Pun 2007; Li et al. 2018). Because enzymatic penetration depends strongly on spheroid size, smaller spheroids can undergo more extensive digestion within the same incubation time, which may artificially enhance staining intensity (Goodman, Olive, and Pun 2007; Im et al. 2019). No differences were observed in samples without matrix degradation, regardless of BSA blocking of non-specific sites. Together, these findings suggest that matrix degradation is a critical prerequisite for efficient antibody binding, in agreement with earlier studies (Didomenico, Lintz, and Bonassar 2018; Goodman, Olive, and Pun 2007; Li et al. 2018).

In contrast to antibodies, small molecule weight dyes such as Hoechst 33342 (616 Da) can readily diffuse through multiple cellular layers and ECM-rich regions with minimal impedance. Previous studies have demonstrated that DNA-binding dyes exhibit rapid and largely matrix-independent penetration kinetics, even in highly compact spheroids, owing to their small size and favorable diffusion properties (Didomenico, Lintz, and Bonassar 2018; Purschke et al. 2010). Consistent with previous reports, the comparable Hoechst 33342 fluorescence intensities observed across all experimental conditions in our study confirm that nuclear staining with this dye is not strongly dependent on pepsin matrix digestion.

However, the duration of enzymatic digestion can also critically influence preservation of the spheroid morphology. While enzymatic treatment can enhance antibody penetration by degrading ECM components, excessive digestion may compromise structural integrity. In the present study, different pepsin incubation times were systematically evaluated to determine an optimal balance between sufficient ECM permeabilization and maintenance of spheroid morphology. However, visual inspection revealed that the 30-minute treatment resulted in partial detachment of peripheral cells, indicating excessive matrix degradation and potential structural damage to the spheroid. Considering both staining efficiency and preservation of spheroid structure, the 20-minute pepsin incubation represented the optimal condition in this experimental setup. These findings highlight the importance of carefully optimizing enzymatic digestion steps in 3D staining protocols, as both insufficient and excessive matrix degradation can negatively affect experimental outcomes (Im et al. 2019).

The third parameter evaluated in our study, i.e. non-specific sites blocking with BSA, yielded similar results to pepsin digestion, demonstrating a significant effect on primary antibody staining intensity, while having no effect on Hoechst 33342 fluorescence. The latter is consistent with earlier reports indicating that Hoechst 33342 exhibits a low propensity for nonspecific interactions with cellular and extracellular components, resulting in stable nuclear labeling regardless of blocking conditions (Purschke et al. 2010). Blocking of nonspecific antigen binding sites is a standard and essential step in immunostaining protocols to enhance signal specificity and reduce background. Among protein-based blocking agents, BSA is one of the most frequently used due to its chemical stability, availability, and effectiveness. BSA is a neutral globular protein that adsorbs to free reactive sites on the substrates and tissue components, thereby preventing nonspecific interactions of antibodies with charged or hydrophobic surfaces (Mondal et al. 2025; Ströhle and Li 2023; Im et al. 2019). In addition, BSA has been reported to reduce electrostatic and hydrophobic antibody binding, which is particularly relevant in protein-rich or highly charged biological matrices.

 doi:10.20944/preprints202604.1558.v1

In the present study, no differences or increases in AF 488 signal intensity were observed following 45 minutes compared to 30 minutes BSA incubation. Notably, smaller spheroids showed no difference in AF 488 signal intensity between the two incubation times, whereas larger spheroids exhibited increased AF 488 signal following prolonged BSA incubation. This lack of change in smaller spheroids, together with the signal increase observed in larger spheroids, suggests that a 45-minute BSA incubation enhances the binding efficiency of the AF 488-conjugated anti-type II collagen antibody primarily in larger spheroids. In theory, shorter blocking durations might be expected to yield higher fluorescence signals due to increased nonspecific antibody binding, potentially resulting in artificially elevated AF 488 intensity. However, this assumption does not fully account for the structural and compositional properties of chondrogenic spheroids with a dense ECM. In such environments, antibody diffusion is limited, as antibodies may engage in transient, nonspecific interactions with ECM components before reaching their target epitopes (Didomenico, Lintz, and Bonassar 2018). Extended BSA incubation likely mitigates this diffusion limitation by more thoroughly saturating nonspecific binding sites within ECM. This enhanced blocking reduces transient antibody–matrix interactions, thereby facilitating deeper and more uniform antibody penetration. As a result, epitope accessibility is improved, leading to increased specific binding of the antibody and a corresponding enhancement of the AF 488 signal. Consistent with our findings, previous studies have shown that optimized blocking conditions improve antibody penetration and signal specificity in dense tissue and hydrogel-based systems (Ströhle and Li 2023; Im et al. 2019).

Interestingly, the next tested parameter, the cell membrane permeabilization with Triton X-100, resulted in enhanced staining with both AF 488 and Hoechst 33342. Triton X-100 is a commonly used membrane–permeabilizing detergent that non-selectively extracts proteins in immunofluorescence protocols (Shahid, Iftikhar, and Simjee 2025). In principle, the permeabilization should not be required in our study, as collagen is synthesized and secreted by chondrocytes into ECM (Siadat and Ruberti 2023). Moreover, Hoechst 33342 is a small DNA intercalating dye that readily enters nuclei without membrane disruption (Didomenico, Lintz, and Bonassar 2018; Purschke et al. 2010). However, increased AF 488 signal in permeabilized samples may be explained by intracellular labelling of procollagen, which is synthesized within the cell prior to secretion. Triton X-100 likely facilitates antibody access to intracellular procollagen, thereby increasing overall signal intensity (Shahid, Iftikhar, and Simjee 2025). Similarly, reduced Hoechst 33342 signal in the absence of Triton X-100 may reflect its limited membrane permeability, whereas permeabilization enables faster nuclear access and greater dye intercalation within the Hoechst 33342 staining time.

During staining of one of the control samples, structural disruption occurred within the Triton X-100 permeabilization step. A plausible explanation is that the ECM of controls (spheroids not treated with chondrogenic media) is mechanically less robust than that of treated samples, i.e. spheroids treated with chondrogenic media (Gonzalez-Fernandez et al. 2022; Omelyanenko et al. 2018; Vakhrushev et al. 2024), rendering it more susceptible to enzyme- and detergent-induced weakening and mechanical stress (Mendibil et al. 2020). As Triton X-100 is used in multiple steps of the protocol, reducing exposure time or omitting selected steps my help minimize such disruption in spheroids with less dense ECM (Mendibil et al. 2020; Gonzalez-Fernandez et al. 2022; Omelyanenko et al. 2018; Vakhrushev et al. 2024). Overall, the current protocol may be overly aggressive for non-chondrogenic or weakly organized matrix tissues, potentially contributing to the observed separation.

Next parameter tested, i.e. the nuclear staining using Hoechst 33342 incubation resulted in no substantial improvement of staining efficiency when incubation time was prolonged from 20 to 60 minutes, based on normalized fluorescence intensity values, suggesting that dye penetration likely reaches an effective equilibrium within 20 minutes under the tested conditions. This is consistent with the notion that diffusion of small-molecule dyes, such as Hoechst 33342 into 3D spheroid models is relatively rapid and may not benefit from prolonged exposure time (Didomenico, Lintz, and Bonassar 2018; Purschke et al. 2010). Overall, these findings suggest that increasing the incubation time does

 doi:10.20944/preprints202604.1558.v1

not improve nuclear staining efficiency, and that a 20-minute incubation is sufficient for reliable staining of spheroids while minimizing experimental time.

Finally, we evaluated the optimized immunofluorescence protocol for its ability to discriminate type II collagen content in spheroids undergoing chondrogenic differentiation compared with control spheroids cultured in the absence of chondrogenic induction. The normalized AF 488 fluorescence intensity was approximately 3-fold higher in the treated samples than in the control, indicating a substantially enhanced deposition of collage type II in response to chondrogenic stimulation. Increased type II collagen production is a well-established hallmark of differentiation and reflects the acquisition and maintenance of a chondrocyte-like extracellular matrix phenotype (Čamernik, Mihelič, Mihalič, Haring, et al. 2020; Čamernik, Mihelič, Mihalič, Marolt Presen, et al. 2020; Haring and Zupan 2022; J. M. Murphy et al. 2002; Zuliani et al. 2024; Zupan and Stražar 2024; M. P. Murphy et al. 2020). A reduction in the Hoechst 33342 fluorescent nuclear signal was observed in control spheroids. This difference is attributed to partial structural disruption of control spheroids, which likely improved dye penetration and resulted in more homogeneous and intense nuclear staining. Similar effects of spheroid architecture on nuclear dye accessibility have been reported in 3D culture systems and are consistent with our observations in other samples of comparable size and cellular density (Zuliani et al. 2024). Taking together, these results demonstrate that this staining and detection protocol can distinguish chondrogenically differentiated samples from their controls in 3D in vitro settings.

5. Conclusions

In conclusion, this study establishes a robust and reproducible immunofluorescence staining and high-content imaging workflow for the quantitative assessment of chondrogenesis in 3D spheroid models derived from primary cells. Through systematic optimization of key experimental parameters, including staining platform, enzymatic matrix digestion, non-specific sites blocking, membrane permeabilization, and nuclear staining we identified conditions that enable efficient antibody penetration, high signal specificity, and preservation of spheroid morphology. Controlled pepsin-mediated matrix digestion and extended BSA blocking emerged as particularly critical determinants for achieving homogeneous and reliable detection of type II collagen within dense, ECM-rich spheroids.

Importantly, coupling the optimized staining protocol with automated high-content confocal imaging allows rapid, quantitative, and scalable analysis of large spheroid cohorts while accounting for spheroid size–dependent effects through normalization strategies. This integrated approach enables sensitive discrimination between type II collagen rich spheroids and controls, demonstrating its suitability for comparative analyses across experimental conditions, tissue sources, and donor-specific primary cells.

Overall, the presented method addresses a key methodological gap in 3D cartilage tissue analytics by providing a fast, standardized, and high-throughput platform for evaluating the chondrogenic potential in vitro. As such, it represents a practical tool for cartilage tissue engineering research and offers clear translational relevance for potency assessment, quality control, and early-stage screening of cell-based ATMPs targeting cartilage repair.

Author Contributions: Conceptualization, L.V., T.B., M.K. and M.J.; methodology, L.V. and T.B.; software, L.V. and T.B.; validation, L.V. and T.B.; formal analysis, L.V. and T.B.; investigation, L.V. and T.B.; resources, M.J., M.K, J.Z and A.T.B.; data curation, L.V. and T.B.; writing—original draft preparation, L.V., T.B. and J.Z.; writing— L.V.,T.B., M.K., M.J. and A.T.B.; visualization, L.V. and T.B.; supervision, M.J., M.K., J.Z. and A.T.B.; project administration, M.K., M.J., J.Z. and A.T.B.; funding acquisition, M.J, J.Z. and A.T.B. All authors have read and agreed to the published version of the manuscript.

Funding: This research was funded by the Slovenian Research and Innovation Agency, Research Projects L3-3176 and Research Program P1-0420, University Medical Centre Ljubljana, Research Project “Evaluation of the properties of primary cells from various perinatal tissues for use in regenerative medicine” (PI Andreja Trojner

 doi:10.20944/preprints202604.1558.v1

Bregar) and IC EATRIS (I0-E011-2022). The Article Processing Charge was funded by University Medical Centre Ljubljana, Research Project "Evaluation of the properties of primary cells from various perinatal tissues for use in regenerative medicine" (PI Andreja Trojner Bregar).

Institutional Review Board Statement: The study was conducted in accordance with the Declaration of Helsinki, and approved by National Medical Ethics Committee of the Republic of Slovenia (reference number 0120-268/2020/3)

Informed Consent Statement: Informed consent was obtained from all subjects.

Data Availability Statement: The original data presented in the study are openly available in Repository of the University of Ljubljana at https://repozitorij.uni-lj.si/info/index.php/eng/.

Acknowledgments: Authors would like to sincerely thank Rok Pangeršič, MD for providing the cartilage samples, and Dr. Dunja Urbančič, MPharm for scientific support in using Revvity Operetta® CLS™ system. During the preparation of this manuscript, the author(s) used M365 Copilot, Microsoft, 2026, https://www.microsoft.com for the purposes of improving English grammar. The authors have reviewed and edited the output and take full responsibility for the content of this publication.

Conflicts of Interest: The authors declare no conflicts of interest. The funders had no role in the design of the study; in the collection, analyses, or interpretation of data; in the writing of the manuscript; or in the decision to publish the results.

Abbreviations

The following abbreviations are used in this manuscript:

ATMPs	Advanced therapies medicinal products
MSCs	Mesenchymal stem/stromal cells
OA	Osteoarthritis
2D	Two-dimensional
3D	Three-dimensional
PBS	Phosphate buffered saline
BSA	Bovine serum albumin
ECM	Extracellular matrix
AF 488	Alexa Fluor 488

References

Čamernik, Klemen, Anže Mihelič, Rene Mihalič, Gregor Haring, Simon Herman, Darja Marolt Presen, Andrej Janež, Rihard Trebše, Janja Marc, and Janja Zupan. 2020. "Comprehensive Analysis of Skeletal Muscle- and Bone-Derived Mesenchymal Stem/Stromal Cells in Patients with Osteoarthritis and Femoral Neck Fracture." *Stem Cell Research and Therapy* 11 (1): 1–14. https://doi.org/10.1186/s13287-020-01657-z.

Čamernik, Klemen, Anže Mihelič, Rene Mihalič, Darja Marolt Presen, Andrej Janež, Rihard Trebše, Janja Marc, and Janja Zupan. 2020. "Increased Exhaustion of the Subchondral Bone-Derived Mesenchymal Stem/Stromal Cells in Primary versus Dysplastic Osteoarthritis." *Stem Cell Reviews and Reports*. https://doi.org/10.1007/s12015-020-09964-x.

Campos, Yaima, Amisel Almirall, Gastón Fuentes, Hans L. Bloem, Eric L. Kaijzel, and Luis J. Cruz. 2019. "Tissue Engineering: An Alternative to Repair Cartilage." *Tissue Engineering - Part B: Reviews* 25 (4): 357–73. https://doi.org/10.1089/ten.teb.2018.0330.

Didomenico, Chris D., Marianne Lintz, and Lawrence J. Bonassar. 2018. "Molecular Transport in Articular Cartilage - What Have We Learned from the Past 50 Years?" *Nature Reviews. Rheumatology* 14 (7): 393–403. https://doi.org/10.1038/s41584-018-0033-5.

Fennema, Eelco, Nicolas Rivron, Jeroen Rouwkema, Clemens van Blitterswijk, and Jan De Boer. 2013. "Spheroid Culture as a Tool for Creating 3D Complex Tissues." *Trends in Biotechnology* 31 (2): 108–15. https://doi.org/10.1016/j.tibtech.2012.12.003.

 doi:10.20944/preprints202604.1558.v1

Gonzalez-Fernandez, Tomas, Alejandro J. Tenorio, Augustine M. Saiz, and J. Kent Leach. 2022. "Engineered Cell-Secreted Extracellular Matrix Modulates Cell Spheroid Mechanosensing and Amplifies Their Response to Inductive Cues for the Formation of Mineralized Tissues." *Advanced Healthcare Materials* 11 (10). https://doi.org/10.1002/adhm.202102337.

Goodman, Thomas T, Peggy L Olive, and Suzie H Pun. 2007. "Increased Nanoparticle Penetration in Collagenase-Treated Multicellular Spheroids." *International Journal of Nanomedicine* 2 (2): 265. https://pmc.ncbi.nlm.nih.gov/articles/PMC2673974/.

Haring, Gregor, and Janja Zupan. 2022. "Knee and Peri-Knee Tissues of Post Mortem Donors Are Strategic Sources of Mesenchymal Stem/Stromal Cells for Regenerative Procedures." *International Journal of Molecular Sciences* 23 (6). https://doi.org/10.3390/IJMS23063170.

Im, Kyuseok, Sergey Mareninov, M. Fernando Palma Diaz, and William H. Yong. 2019. "An Introduction to Performing Immunofluorescence Staining." *Methods in Molecular Biology (Clifton, N.J.)* 1897: 299–311. https://doi.org/10.1007/978-1-4939-8935-5_26.

Li, Ang, Yiyong Wei, Clark Hung, and Gordana Vunjak-Novakovic. 2018. "Chondrogenic Properties of Collagen Type XI, a Component of Cartilage Extracellular Matrix." *Biomaterials* 173 (August): 47–57. https://doi.org/10.1016/j.biomaterials.2018.05.004.

Mendibil, Unai, Raquel Ruiz-Hernandez, Sugoi Retegi-Carrion, Nerea Garcia-Urquia, Beatriz Olalde-Graells, and Ander Abarrategi. 2020. "Tissue-Specific Decellularization Methods: Rationale and Strategies to Achieve Regenerative Compounds." *International Journal of Molecular Sciences* 21 (15): 5447. https://doi.org/10.3390/ijms21155447.

Mondal, Atanu, Sandhik Nandi, Bipasa Mandal, Indrakshi Banerjee, Md Wasim Akram Ddoza Hazari, and Chandrima Das. 2025. "Protocol for 3D Tumor Spheroid Generation, Immunostaining, and Imaging through Comparative Approaches." *STAR Protocols* 6 (4). https://doi.org/10.1016/j.xpro.2025.104168.

Murphy, J. Mary, Kenneth Dixon, Stephen Beck, Dennis Fabian, Andrew Feldman, and Frank Barry. 2002. "Reduced Chondrogenic and Adipogenic Activity of Mesenchymal Stem Cells from Patients with Advanced Osteoarthritis." *Arthritis and Rheumatism* 46 (3): 704–13. https://doi.org/10.1002/art.10118.

Murphy, Matthew P., Lauren S. Koepke, Michael T. Lopez, Xinming Tong, Thomas H. Ambrosi, Gunsagar S. Gulati, Owen Marecic, et al. 2020. "Articular Cartilage Regeneration by Activated Skeletal Stem Cells." *Nature Medicine* 26 (10): 1583–92. https://doi.org/10.1038/s41591-020-1013-2.

Omelyanenko, Nikolai P., Pavel A. Karalkin, Elena A. Bulanova, Elizaveta V. Koudan, Vladislav A. Parfenov, Sergei A. Rodionov, Alisa D. Knyazeva, et al. 2018. "Extracellular Matrix Determines Biomechanical Properties of Chondrospheres during Their Maturation In Vitro." *Cartilage* 11 (4): 521. https://doi.org/10.1177/1947603518798890.

"Osteoarthritis." n.d. Accessed April 1, 2026. https://www.who.int/news-room/fact-sheets/detail/osteoarthritis/.

Partridge, Linda, Joris Deelen, and P. Eline Slagboom. 2018. "Facing up to the Global Challenges of Ageing." *Nature* 561 (7721): 45–56. https://doi.org/10.1038/s41586-018-0457-8.

Purschke, Martin, Noemi Rubio, Kathryn D. Held, and Robert W. Redmond. 2010. "Phototoxicity of Hoechst 33342 in Time-Lapse Fluorescence Microscopy." *Photochemical & Photobiological Sciences 2010 9:12* 9 (12): 1634–39. https://doi.org/10.1039/C0PP00234H.

Qiao, Lichun, Miaoqian Li, Feidan Deng, Xinyue Wen, Huan Deng, Zhaowei Xue, Jingxuan Zhou, et al. 2025. "Epidemiological Trends of Osteoarthritis at the Global, Regional, and National Levels from 1990 to 2021 and Projections to 2050." *Arthritis Research & Therapy 2025 27:1* 27 (1): 199-. https://doi.org/10.1186/s13075-025-03658-w.

Shahid, Maha, Kanwal Iftikhar, and Shabana Usman Simjee. 2025. "Impact of Triton X-100 on Notch 1 Surface Receptor Immunofluorescence: A Cautionary Study." *Discoveries* 13 (1): e206. https://doi.org/10.15190/d.2025.5.

Siadat, Seyed Mohammad, and Jeffrey W. Ruberti. 2023. "Mechanochemistry of Collagen." *Acta Biomaterialia* 163 (June): 50–62. https://doi.org/10.1016/j.actbio.2023.01.025.

Ströhle, Gisela, and Huiyan Li. 2023. "Comparison of Blocking Reagents for Antibody Microarray-Based Immunoassays on Glass and Paper Membrane Substrates." *Analytical and Bioanalytical Chemistry* 415 (10): 1967–77. https://doi.org/10.1007/S00216-023-04614-W.

 doi:10.20944/preprints202604.1558.v1

Vakhrushev, Igor V., Yulia B. Basok, Konstantin K. Baskaev, Victoria D. Novikova, Georgy E. Leonov, Alexey M. Grigoriev, Aleksandra D. Belova, et al. 2024. "Cartilage-Specific Gene Expression and Extracellular Matrix Deposition in the Course of Mesenchymal Stromal Cell Chondrogenic Differentiation in 3D Spheroid Culture." *International Journal of Molecular Sciences* 25 (11). https://doi.org/10.3390/ijms25115695.

Žigon-Branc, Sara, Ariana Barlič, Miomir Knežević, Matjaž Jeras, and Gordana Vunjak-Novakovic. 2018. "Testing the Potency of Anti-TNF-α and Anti-IL-1β Drugs Using Spheroid Cultures of Human Osteoarthritic Chondrocytes and Donor-Matched Chondrogenically Differentiated Mesenchymal Stem Cells." *Biotechnology Progress* 34 (4): 1045–58. https://doi.org/10.1002/BTPR.2629.

Zuliani, Carolina C., Larissa H. Teixeira, Jessica B. da Cunha, Angela M. Moraes, and Ibsen B. Coimbra. 2024. "Chondrogenic Differentiation Efficacy in Micromolded Spheroids Generated From Mesenchymal Stem Cells Isolated From Amniotic Fluid and Dental Pulp: A Comparative Analysis." *Osteoarthritis and Cartilage* 32: S310–11. https://doi.org/10.1016/j.joca.2024.02.454.

Zupan, Janja, and Klemen Stražar. 2024. "Synovium-Derived and Bone-Derived Mesenchymal Stem/Stromal Cells from Early OA Patients Show Comparable In Vitro Properties to Those of Non-OA Patients." *Cells* 13 (15): 1238. https://doi.org/10.3390/CELLS13151238/S1.

Zupan, Janja, Klemen Strazar, Roland Kocijan, Thomas Nau, Johannes Grillari, and Darja Marolt Presen. 2021. "Age-Related Alterations and Senescence of Mesenchymal Stromal Cells: Implications for Regenerative Treatments of Bones and Joints." *Mechanisms of Ageing and Development* 198 (September). https://doi.org/10.1016/j.mad.2021.111539.